Numerical Simulation of Low and Medium Power Arcjet Thrusters

IEPC-2011-153

Presented at the 32nd International Electric Propulsion Conference,
Wiesbaden • Germany
September 11 – 15, 2011

Fu-Zhi Wei[1] and Hai-Xing Wang[2]
Beijing University of Aeronautics and Astronautics, Beijing, 100191, China

E. Y. Choueiri[3]
Electric Propulsion and Plasma Dynamics Laboratory, Princeton University, Princeton, New Jersey, 08540, US

Abstract: Modeling studies are conducted to investigate the plasma flow, heat transfer and energy conversion characteristics of low and medium power arcjet thrusters with hydrogen as the propellant. In order to better treat the conjugate heat transfer between the gas flow region and the solid wall region, the anode is included in the computational domain. A code based on finite difference Roe-type scheme is developed to solve the set of governing equations. Modeling results are found to compare favorably with available experimental data for three arcjet thrusters with different power levels. The axial variations of the enthalpy flux, kinetic energy flux, directed kinetic-energy flux and total enthalpy flux are used to investigate the energy conversion process inside the thruster nozzle. The effects of power on the flow, heat transfer, and energy conversion processes within three thrusters are discussed.

Nomenclature

B_θ = magnetic induction intensity
$\vec{B}$ = magnetic induction intensity vector
e_t = total energy per unit volume
E = electric field
$\vec{E}$ = electric field vector
h = specific enthalpy
I = arc current
I_{sp} = specific impulse
j = current density
$\vec{j}$ = current density vector
k_B = Boltzmann constant
$\dot{m}$ = the mass flow rate
$\overline{m}$ = the normalized mass flow rate
p = gas static pressure
R = gas constant
T = gas temperature
$\vec{U}$ = the velocity vector

[1] Graduate Student, School of Astronautics, weifuzhi@sa.buaa.edu.cn.
[2] Associate Professor, School of Astronautics, whx@buaa.edu.cn.
[3] Professor, Electric Propulsion and Plasma Dynamics Laboratory, choueiri@princeton.edu.

v = radial velocity
γ = specific-heat ratio
κ = thermal conductivity
μ = viscosity
μ_0 = the magnetic permeability
ρ = gas density
σ = electric conductivity
γ = specific heat ratio
τ = shear stress

I. Introduction

The arcjet is an electrothermal thruster which uses an arc to increase the enthalpy of the propellant which is subsequently thermodynamically expanded by a nozzle to supersonic velocities. The potential saving in satellite propulsion system mass has generated much effort in the development and flight qualification of arcjet thrusters. Although the device has lower specific impulse than those of, for example, MPD or ion thruster, the arcjet is still the choice of propulsion system for the near future due to its compatibility with the present low power levels afforded by satellite electrical systems, and the relative simplicity of the power supply design. Low power 1-2 kW systems are now in use for north-south station keeping of satellites[1], while higher power 20-30 kW designs are being considered for orbit transfer applications[2].

In general, there is no essential difference in main physical processes of the arcjet thrusters operated with different power levels. While moving up in power from 1 kW to 50 kW, the typical arc currents, mass flow rates increase from the order of 10 A, 14.2 mg/s to 400 A, 200 mg/s, respectively, and the representative length of constrictor increases from the order of 0.25 mm to 4 mm. It was also of interest to find out the variations of the thruster performance and some important physical parameters with the power levels of arcjet thrusters. Moreover, in order to remain competitive with the Hall thruster and ion engine for the case of high power space mission, significant increase in the specific impulse of present arcjet technology must be achieved. While the improving performance of arcjet thruster operated at high power requires that a sufficient understanding of the arcjet plasma physics, including the dynamics of arc attachment and some other unsolved issues. In order to better clarify the effect of the power levels on the thruster characteristics, our modeling studies are performed using the hydrogen as the propellant but different thrusters operated with different power levels.

II. Modeling Approach

A. Governing equations

The main assumptions employed in the modeling study are as follows. (i) the gas flow in the arcjet nozzle is steady, axisymmetric, laminar and compressible; (ii) the bulk plasma is in the LTE (local thermodynamic equilibrium) state and thus the thermodynamic and transport properties are completely determined by the gas temperature and pressure[3-5]; non-LTE effects are only considered by appropriately increasing the values of gas electrical conductivity in the low temperature region; (iii) the azimuthal (swirling) velocity component is negligible in comparison with the axial velocity component. Based on these assumptions, the set of governing equations in the cylindrical coordinate system can be written as follows

$$\frac{\partial}{\partial t}\begin{bmatrix}\rho\\ \rho u\\ \rho v\\ \rho e_t\end{bmatrix}+\frac{\partial}{\partial z}\begin{bmatrix}\rho u\\ \rho u^2+p\\ \rho uv\\ \rho uH\end{bmatrix}+\frac{\partial}{\partial r}\begin{bmatrix}\rho v\\ \rho uv\\ \rho v^2+p\\ \rho vH\end{bmatrix}+\frac{1}{r}\begin{bmatrix}\rho v\\ \rho uv\\ \rho v^2\\ \rho vH\end{bmatrix}=\frac{\partial}{\partial z}\begin{bmatrix}0\\ \tau_{zz}\\ \tau_{zr}\\ u\tau_{zz}+v\tau_{zr}-q_z\end{bmatrix}+\frac{\partial}{\partial r}\begin{bmatrix}0\\ \tau_{rz}\\ \tau_{rr}\\ u\tau_{rz}+v\tau_{rr}-q_r\end{bmatrix} \quad (1)$$
$$+\frac{1}{r}\begin{bmatrix}0\\ \tau_{zr}-\frac{2}{3}r\frac{\partial}{\partial z}(\mu\frac{v}{r})\\ \tau_{rr}-\tau_{\theta\theta}-\frac{2}{3}\mu\frac{v}{r}-\frac{2}{3}r\frac{\partial}{\partial r}(\mu\frac{v}{r})\\ u\tau_{zr}+v\tau_{rr}-q_r-\frac{2}{3}\mu\frac{v^2}{r}-\frac{2}{3}r\frac{\partial}{\partial r}(\mu\frac{v^2}{r})-\frac{2}{3}r\frac{\partial}{\partial z}(\mu\frac{uv}{r})\end{bmatrix}+\begin{bmatrix}0\\ j_rB_\theta\\ -j_zB_\theta\\ j_zE_z+j_rE_r\end{bmatrix}$$

where

$$\rho e_t = \rho\left(u^2 + v^2\right)/2 + p/(\gamma - 1), \quad \rho H = \rho e_t + p, \quad \tau_{zz} = \mu\left(4\partial u/\partial z - 2\partial v/\partial r\right)/3,$$
$$\tau_{rr} = \mu\left(4\partial v/\partial r - 2\partial u/\partial z\right)/3, \quad \tau_{zr} = \tau_{rz} = \mu\left(\partial v/\partial z + \partial u/\partial r\right), \quad \tau_{\theta\theta} = \mu\left(-2(\partial v/\partial r + \partial u/\partial z) + 4v/r\right)/3,$$
$$q_z = -\kappa\partial T/\partial z, \quad q_r = -\kappa\partial T/\partial r$$

The electromagnetic equations involved in this study are described as

$$\vec{j} = \sigma(\vec{E} + \vec{U} \times \vec{B}) \qquad \nabla \times \vec{E} = 0, \qquad \nabla \times \vec{B} = \mu_0 \vec{j} \tag{2}$$

Equation (2) are the general Ohm's law ignoring the terms of electron pressure gradient and the Hall current, steady-state Farady's law and Ampre's law, respectively. From equation (2), the following elliptic equation is derived with respect to azimuthal magnetic field B_θ in the cylindrical coordinate system.

$$\frac{\partial}{\partial r}\left[\frac{1}{r\sigma}\frac{\partial(rB_\theta)}{\partial r}\right] + \frac{\partial}{\partial z}\left[\frac{1}{r\sigma}\frac{\partial(rB_\theta)}{\partial z}\right] = \mu_0\left[\frac{\partial(vB_\theta)}{\partial r} + \frac{\partial(uB_\theta)}{\partial z}\right] \tag{3}$$

After B_θ has been obtained, the current density and electric field can be determined by equation (2).

It is found in previous studies that most of the incoming gaseous propellant flows towards the nozzle exit through the outer cooler region near the anode-nozzle wall. Since the inner-surface temperatures of the anode-nozzle wall directly affect the gas temperatures and velocities in the near-wall region and thus affect the thrust force and specific impulse of the arcjet thruster, accurate calculation of the temperature distribution along the inner-surface of the thruster nozzle is important. In this study the anode-nozzle wall is included in the computational domain. Neglecting the Joule heating in the anode, the problem is governed by the following equation in the cylindrical coordinate

$$\frac{\partial}{\partial z}(\kappa\frac{\partial T}{\partial z}) + \frac{\partial}{\partial r}(\kappa\frac{\partial T}{\partial r}) + \frac{1}{r}\kappa\frac{\partial T}{\partial r} = 0 \tag{4}$$

B. Numerical scheme

In this study, Roe scheme[6] with MUSCL limiters, a well-known scheme in solving hyperbolic systems of conservation for its ability of capturing discontinuity, is introduced to discretize the convection terms in equation (1), and the diffusion terms are discretized by a central-differencing scheme. A fourth-order Runge-Kutta scheme is chosen to march forward in time. And the ADI scheme is employed to solve Eq. (3) and (4) in every time step.

It is noted that all the partial derivatives are expressed in physical space. In order to solve the governing equations in the computational space, a transformation of the equations from physical space into computational space is required before solving the governing equations.

C. Boundary conditions

Modelling studies are conducted from the low power arcjet (~1 kW) to the medium-high power cases (~46 kW). The construction and geometrical sizes of the low power arcjet thruster is almost the same with the radiation-cooled arcjet thruster designed by NASA Lewis Research Center, which is called Thruster A hereafter. The other two types of medium-high power radiation-cooled arcjet thrusters designed by University of Stuttgart are also used in the present modelling study in order to compare the modelling prediction with the experimental data available in the literature[7,8]; they will be called Thruster B and C. The geometrical sizes of the arcjet thrusters are listed in Table 1.

Table 1. The geometrical sizes of the three thrusters

Thruster	A	B	C
Upstream anode half-angle (º)	30	50	50
Cathode diameter (mm)	3.0	4.0	10.0
Cathode tip angle(º)	30	30	30
Constrictor diameter (mm)	0.635	2.5	4.0
Constrictor length (mm)	0.25	5.0	4.0
Nozzle half-angle(º)	20.0	17.5	20.0
Nozzle length (mm)	12.15	35.7	77.0
Exit diameter (mm)	9.53	25.0	60.0
Area ratio of exit to constrictor	1:225	1:100	1:225

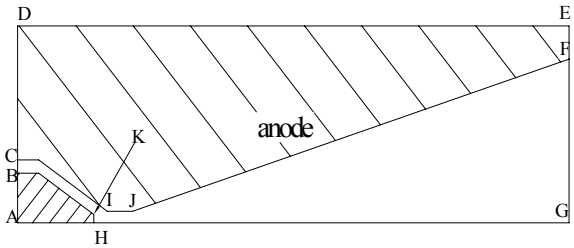

Figure 1. Schematic diagrams of Thruster A.

Table 2. Boundary conditions

	B-C	C-I-J-F	F-G	G-H	H-K-B
Flow Field	p: extrapolated v, T: specified u: from $\dot{m}$	p: dp/dn=0 u= v =0 T: $\kappa_{Anode}(dT/dn)_{Anode}=\kappa_{Gas}(dT/dn)_{Gas}$	p, u, v, T : extrapolated	p: dp/dr=0 u: du/dr=0 v =0 T: dT/dr=0	p: dp/dn=0 u= v =0 T: specified
	B-C-I-J	J-F	F-G-H	H-K	K-B
Magnetic Field	$rB_\theta=-\mu_0 I/(2\pi)$	$\partial(rB_\theta)/\partial r \cos\varphi - \partial(rB_\theta)/\partial z \sin\varphi=0$ (φ: Nozzle half-angle)	$rB_\theta=0$	rB_θ diminishes from 0 to $-\mu_0 I/(2\pi)$	$rB_\theta=-\mu_0 I/(2\pi)$
	D-C	C-I-J-F	F-E		E-D
Anode	dT/dn=0	$\kappa_{Anode}(dT/dn)_{Anode}=\kappa_{Gas}(dT/dn)_{Gas}$	$-\kappa\, dT/dn=\varepsilon\sigma T^4$		$-\kappa\, dT/dn=\varepsilon\sigma T^4$

For the purpose of detailed description of boundary conditions, Thruster A is taken as an example and its schematic diagram is shown in Fig. 1. The boundary conditions for Thruster B and C are similar. Due to the axisymmetry of the thruster, only the upper half of the thruster is taken into account in the computation. The computational domain used in the modeling for is denoted as B-C-D-E-F-G-H-K-B, in which B-C-I-J-F-G-H-K-B is the boundary of gas domain, and C-D-E-F-J-I-C is the anode-nozzle wall, whereas C-I, I-J and J-F are the inner surfaces of the convergent segment, cylindrical segment (constrictor) and divergent segment of the anode-nozzle. The boundary conditions used in the computation are summarized in Table 2.

III. Results and Discussion

A. Comparisons of predicted results and experimental results

Each thruster is computed at its typical working condition with hydrogen as the propellant. Comparison of predicted results and experimental results is given in Table 3.

Table 3. Comparison of predicted results and experimental results

Thruster	A		B		C	
	predicted	Experimental[9]	predicted	Experimental[8]	predicted	Experimental[7]
Mass Flow Rate (mg/s)	14.2	13.0	100	100	200	200
Current (A)	10.0	10.3	140	140	400	400
Power (kW)	1.25	1.43	13.3	15.4	36.6	~46
Thrust (N)	0.111	0.106	1.135	1.07	2.57	~2.5
Specific Impulse (s)	797	830	1157	1090	1311	~1276

Since the sheath model is not included in our modeling, the predicted powers of arcjert thruster in Table 3 are reasonably lower than the corresponding experimental results. And the predicted thrust and specific impulse are consistent with the experimental data, which means our code can predict well the overall performance of the arcjet thruster from a low power level (1.43 kW) to a medium-high power level(~46 kW).

A further comparison is made to validate the accuracy of the code used in our study with experimental results of hydrogen arcjet thruster reported by Cappelli and his co-workers[9-14]. The predicted results for the axial-velocity variation along the nozzle axis and the radial profiles of the axial velocity at the exit of Thruster A are compared with their corresponding experimental data in Fig. 2. It can be seen that in Fig. 2(a) predicted axial variation of the axial velocity along the nozzle axis agrees well with the corresponding experimental data[13], and in Fig. 2(b) the agreement between the experimental[9] and predicted results is fair in the central part of the jet, while the discrepancy becomes appreciable in the fringe region, probably due to the existence of rarefaction gas effects near the anode-nozzle wall.

From the foregoing comparison, although LTE is assumed, with the only non-LTE effect included being an increased gas electrical conductivity in the low temperature region, the modeling predictions are reasonably consistent with available experimental results for hydrogen arcjet thrusters.

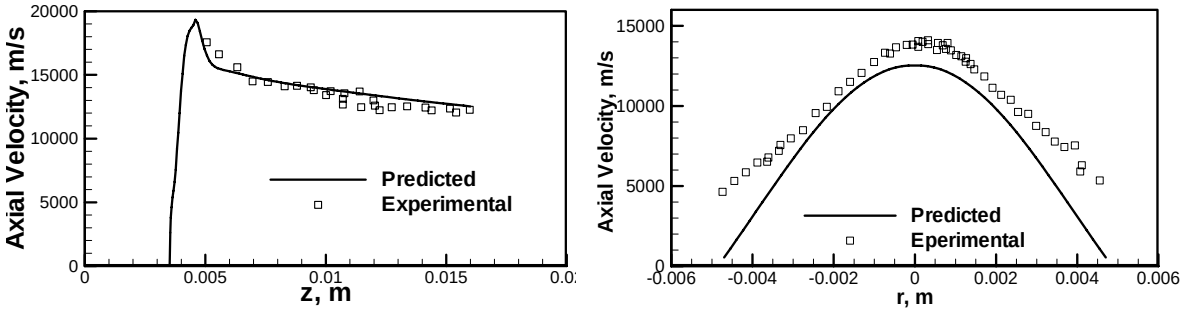

(a) axial velocity along nozzle axis **(b) axial velocity at the exit plane**

Figure 2. Comparisons of the predicted results and the experimental data[9,13] for Thruster A.

B. Flow fields

Figure 3 plots the computed temperature distributions in the gas flow region of the thrusters, showing that the temperature distributions within the thruster are similar overall for the three different thrusters. The gaseous propellant entering into the thruster undergoes a rapid temperature rise in the near-cathode and constrictor region due to arc heating (Joule heating). Subsequently the heated high temperature partially-ionized gas (plasma) expands in the diverging part of the nozzle, accompanying by an appreciable temperature decrease in the axial direction in the nozzle. There exist large radial gradients of the gas temperature in the thruster nozzle, especially in the constrictor region. The high temperature region appearing nearby the constrictor only occupies a small volume. And this volume increase with the increase of the power of arcjet thruster, as is expected.

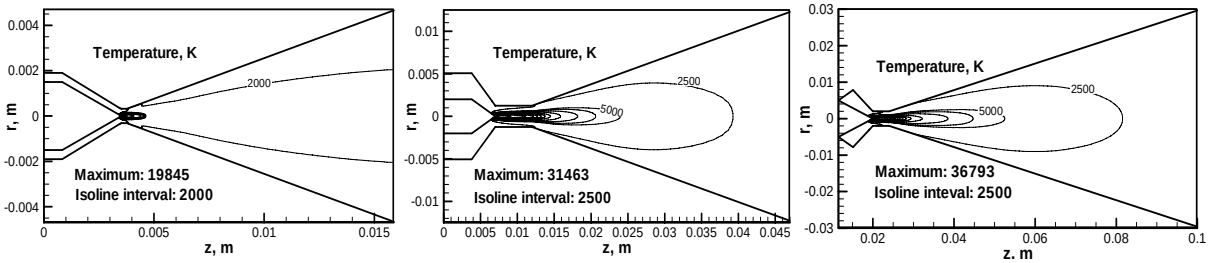

(a) Thruster A, 1.43 kW **(b)Thruster B, 15.4 kW** **(c) Thruster C, 46 kW**

Figure 3. Computed temperature contours within the gas flow region.

The computed axial velocity distributions within the thrusters are shown in Fig. 4. Overall the axial velocity distributions are also similar for the three different thrusters. Figure 4 shows that due to the conversion of the pressure energy and internal energy into the kinetic energy, the gaseous propellant flowing into the nozzle is rapidly accelerated to rather high velocities within a short axial distance. There exist large radial gradients of the axial velocity in the thrusters. Unlike the conventional compressible flow in a Laval nozzle, the maximum velocity is found to appear in the interior of the arcjet nozzle (at the location near the downstream end of the constrictor) instead of at the nozzle exit. This phenomenon has been observed in experiments[10,11] and is believed to be due to the complex interaction between the Joule heating, Lorentz force, viscous force and thermodynamic expansion in the constrictor and near-constrictor region.

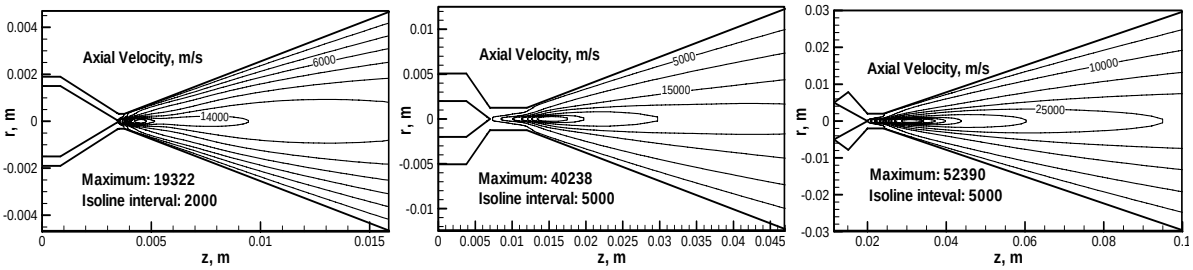

(a) Thruster A, 1.43 kW **(b)Thruster B, 15.4 kW** **(c) Thruster C, ~46 kW**

Figure 4. Computed axial velocity contours within the gas flow region.

Fig. 5 compares the computed variations along the nozzle axis of the plasma temperature and axial velocity for the three arcjet thrusters. In order to plot the variations for three thrusters of different geometrical sizes in one figure, the axial coordinate is normalized by their own distance from cathode tip to exit of the thruster. Fig. 5(a) clearly shows that the on-axis temperature increases very rapidly to its maximum value due to the arc heating in the near-cathode and constrictor region, and then decreases quite rapidly to comparatively low values as the hot gas expands in the divergent segment of the nozzle. The highest plasma temperatures appearing in the rapid-heating region are 19845, 31463 and 36793 K, respectively, for Thruster A, B and C. Fig. 5(b) shows that the axial velocity distributions along the thruster axis increases rapidly at first until a maximum is achieved, and then decreases gradually as the propellant flows towards the thruster exit. In the divergent segment of the thruster nozzle, the axial velocities at the nozzle axis decrease from the maximum values of 19322, 40238 and 52390 to 12530, 21529 and 24516 m/s at the exit, respectively, for Thruster A, B and C. For Thruster A, the predicted axial variation of axial velocity is consistent with the measurements as shown in Fig. 2. Since there are no published experimental data concerning axial velocity distribution, no further direct comparisons for Thruster B and C can be made. But there is an indirect way to validate the predicted results. As discussed before, the predicted thrust agrees with the experimental data, as shown in Table 3. If the conservation of mass flow rate is achieved, it can be concluded that the predicted axial velocity should be reasonable according to the relation between the axial velocity and thrust. The variations of mass flow rates with the axial distance in Thruster B and C are given in Fig. 6. It can be seen that the mass flow rates in Thruster B and C are almost kept constant, which means the predicted axial velocities in this study are reasonable.

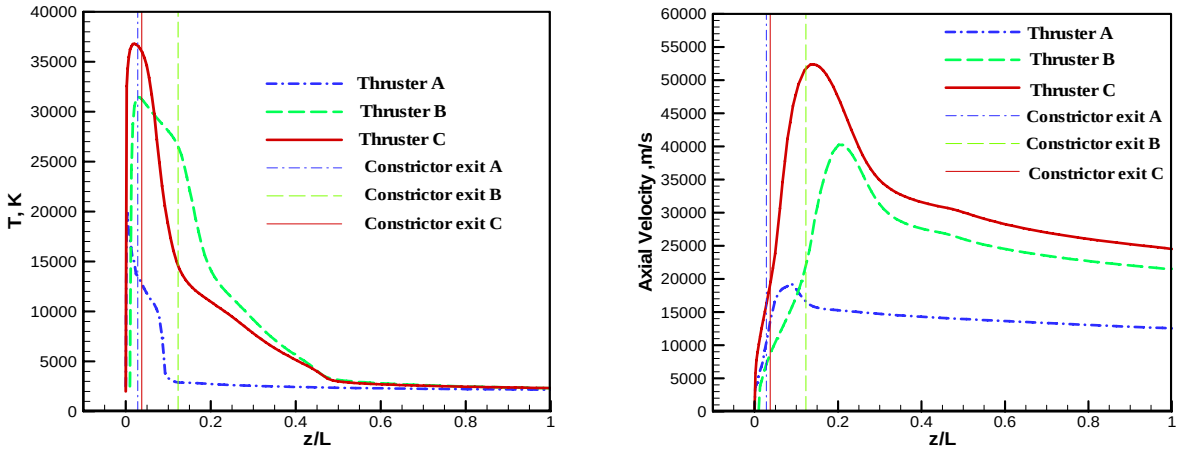

(a) Temperature variations along the axis **(b) Axial velocity variations along the axis**

Figure 5. Comparisons of the computed variations of temperature and axial velocity.

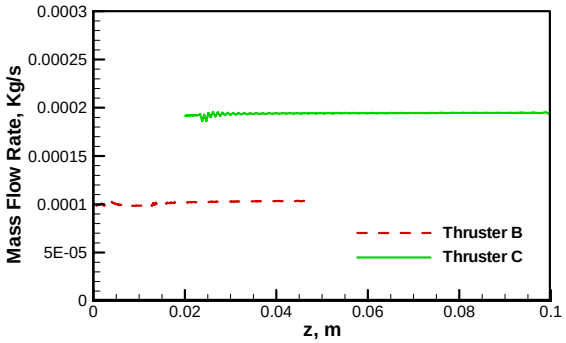

Figure 6. The mass flow rates in Thruster B and C with the axial distance.

Table 4. The maximum temperature and input power density in the three thrusters

Thruster	The maximum temperature (K)	The maximum input power density(W/m^3)
A	19845	4.58×10^{14}
B	31463	5.72×10^{13}
C	36793	1.41×10^{13}

Table 4 lists some important parameters, i.e., the maximum temperatures and input power densities, for the three thrusters. It is interesting to note that the maximum of input power density in Thruster A is the highest among three thrusters while its corresponding maximum of temperature is the lowest. The situation in Thruster C is opposite. These phenomena can be explained as follows.

Fig. 7, within which the radial coordinates are normalized by their own radius of constrictor, plots the radial profiles of temperature, density and normalized mass flow rate at the constrictor inlet. The normalized mass flow rate is defined as

$$\overline{m} = \rho u 2\pi r \Delta r / \dot{m} \tag{5}$$

where Δr is the local radial distance between two adjacent grid points. Fig. 7(a) indicates that Thruster A with the lowest power has the largest high temperature region among the three thrusters, while Thruster C with the highest power has the smallest high temperature region. Correspondingly, low density region in Thruster A is the smallest while the largest in Thruster C, as shown in Fig. 7(b). It further indicates in Fig. 7(C), the most of gaseous propellant easily flows towards the constrictor exit through the outer cooler region near the anode wall, especially for the case of Thruster C with the largest constrictor diameter.

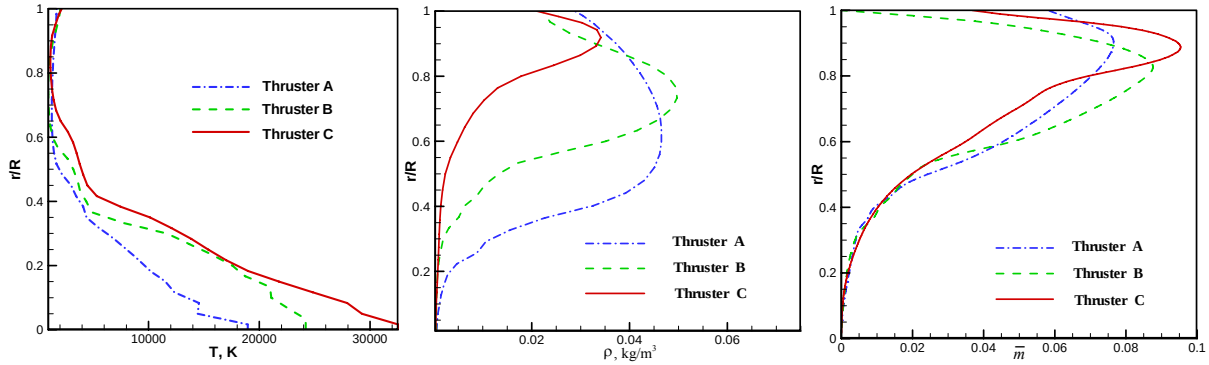

(a) Temperature **(b) Density** **(c) Normalized mass flow rate**

Figure 7. Radial profiles of temperature, density and normalized mass flow rate at the constrictor inlet.

C. Energy conversion

Since the energy conversion within the thruster nozzle determines the performance of arcjet thruster, it would be useful to analyze the effect of gas composition on the energy conversion characteristics. In order to better compare the energy conversion characteristics, a reduced enthalpy flux, E_h, a reduced kinetic energy flux, E_K , a reduced directed kinetic-energy flux, E_{Ka} and the reduced total enthalpy flux E_H are introduced in this study to characterize the energy conversion processes. They are defined as the local enthalpy flux, kinetic energy flux, directed kinetic-energy flux and across a cross-section of the thruster, normalized to the mass flow rate of the propellant flowing in the thruster, i.e

$$E_h = \int \rho u h 2\pi r dr / \dot{m}, \qquad E_K = \int \rho u[0.5(u^2 + v^2)]2\pi r dr / \dot{m}$$
$$E_{Ka} = \int \rho u(0.5u^2)2\pi r dr / \dot{m}, \qquad E_H = E_h + E_K \tag{6}$$

Figure 8 presents the computed variations of E_h, E_K, E_{Ka} and E_H for the three thrusters. The shadow in Figs. 8 represents the constrictor region in the thrusters. It can be seen that trends of each reduced flux for different thruster

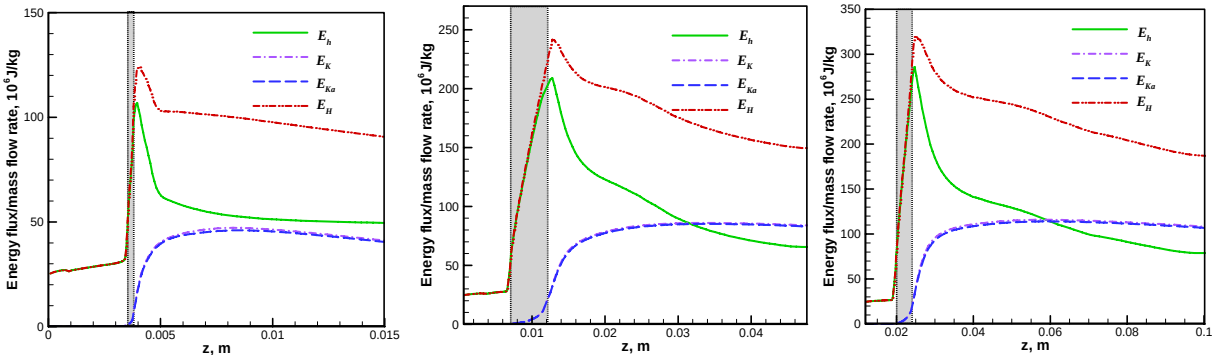

(a) Thruster A **(b) Thruster B** **(c) Thruster C**

Figure 8. Computed axial variations of the enthalpy flux, the kinetic energy flux, directed kinetic-energy flux and the total enthalpy flux, normalized to the mass flow rate.

are similar. As shown in Fig. 8, E_h increases rapidly in the near-cathode and constrictor region due to the arc heating, similarly to the on-axis temperature rise shown in Fig. 5(a). After the maximum value has been achieved, the E_h decreases gradually in the axial direction due to the thermodynamic expansion of propellant in the supersonic nozzle, but its decay rate is appreciably less than that of the on-axis temperature shown in Fig. 5(a), reflecting the effect of heat and momentum transfer in the radial direction in the nozzle. E_K and E_{Ka} increase rapidly at first due to the gas heating and the thermodynamic expansion in the supersonic nozzle and then decrease gradually as the propellant flows towards the nozzle exit due to the energy loss caused by the heat transfer to the nozzle wall and the effect of viscous drag. E_K and E_{Ka} reach their maximum values in the interior of the nozzle. E_{Ka} for a given axial position is only slightly less than corresponding E_K, which is because the radial velocity component in the nozzle is appreciably lower than the axial velocity component, and thus the gas kinetic energy is determined dominantly by the axial velocity component. E_H increases rapidly due to the electric energy input, and after achieving its maximum value it decreases due to heat transfer to the nozzle wall.

IV. Conclusion

Numerical simulations have been carried out to study the plasma flow, heat transfer and energy conversion characteristics of three arcjet thrusters with hydrogen as the propellant. A finite difference Roe-type scheme is developed to solve the set of governing equations. Modeling results are compared with available experimental data and found to compare favorably for the three arcjet thrusters of different power levels. The three thrusters share some common features for the flow, heat transfer, and energy conversion processes. The propellant is heated mainly in the near-cathode and constrictor region, accompanied with a rapid increase of the enthalpy flux, and after achieving its maximum value, the enthalpy flux decreases appreciably due to the conversion of gas internal energy into its kinetic energy in the divergent segment of the thruster nozzle. With the increase of the power, the maximum temperature and axial velocity within different arcjet thrusters also increase.

Acknowledgments

This work was supported by the National Natural Science Foundation of China (Nos. 50836007, 11072020).

References

[1]Sackheim, R. L., "Overview of United States Space Propulsion Technology and Associated Space Transportation Systems," *Journal of Propulsion and Power*, Vol. 22, No. 6, 2006, pp. 1310–1333.

[2]Auweter-Kurtz, M., Glocker, B., Goelz, T., "Arcjet Thruster Development," *Journal of Propulsion and Power*, Vol. 12, No. 6, 1996, pp. 1077-1083.

[3]Murphy, A. B. , Arundell, C. J. "Transport Coefficients of Argon, Nitrogen, Oxygen, Argon-nitrogen, and Argon-oxygen Plasmas," *Plasma Chemistry and Plasma Processing*, Vol. 14, No. 4,1994, pp. 451-490.

[4]Murphy, A. B., "Transport Coefficients of Hydrogen and Argon-hydrogen Plasmas," *Plasma Chemistry and Plasma Processing*, Vol. 20, No. 3, 2000, pp. 279-297.

[5]Chen, X., *Heat Transfer and Fluid Flow under Thermal Plasma Conditions*, 2nd ed., Science Press. Beijing, 2009,Chapter 3 (in Chinese).

[6]Roe, P. L., "Approximate Riemann Solvers, Parameter vectors, and difference Schemes," *Journal of Computational Physics*, Vol. 43, No. 2, 1981, pp. 357–372.

[7]Auweter-Kurtz, M., Glocker, B., Habiger, H., "High-Power Hydrogen Arcjet Thrusters," *Journal of Propulsion and Power*, Vol. 14, No. 5, 1998, pp. 764-773.

[8]Miller, S. A., "Multi-fluid Non-equilibrium Simulation of Arcjet Thrusters," Ph.D. Dissertation, Aeronautics and Astronautics Dept., MIT, Boston, MA, 1994.

[9]Liebeskind, J. G., Hanson, R. K., Cappelli, M. A., "Laser-induced Fluorescence Diagnostic for Temperature and Velocity Measurements in a Hydrogen Arcjet Plume," *Applied Optics*, Vol. 32, No. 30, 1993, pp. 6117-6127.

[10]Cappelli, M. A., Storm, P. V., "Interior Plasma Diagnostics of Arcjet Thrusters," *Journal of Propulsion and Power*, Vol. 12, 1996, pp. 1070–1076.

[11]Storm, P. V.,Cappelli, M. A., "Arcjet Nozzle flow-field Characterization by Laser-induced Fluorescence," *Applied Optics*, Vol. 37, No. 3, 1998, pp. 486–495.

[12]Storm, P. V.,Cappelli, M. A., "Stark Broadening Corrections to Laser-induced Fluorescence Temperature Measurements in A Hydrogen Arcjet Plume," *Applied Optics*, Vol. 35, No. 24, 1996, pp. 4913–4918.

[13]Storm, P. V.,Cappelli, M. A., "Radiative Emission Analysis of An Expanding Hydrogen Arc Plasma—II. Plume Region Diagnostics Through Radial Emission," *Journal of Quantitative Spectroscopy and Radiative Transfer*, Vol. 56, No. 6, 1996, pp. 919–932.

[14]Hirschfelder, J. O., Kurtis, C. F., Bird, R. B., *Molecular Theory of Gases and Liquids*, Wiley, New York, 1964,Chaps. 7. 8. 9.